New functional insights into the internal architecture of the laminated anchor spicules of *Euplectella aspergillum*

Michael A. Monn[a], James C. Weaver[b], Tianyang Zhang[a], Joanna Aizenberg[b,c], and Haneesh Kesari[a,1]

[a]School of Engineering, Brown University, Providence, RI 02912; and [b]Wyss Institute for Biologically Inspired Engineering and [c]School of Engineering and Applied Sciences, Harvard University, Cambridge, MA 02138

Edited by Guy M. Genin, Washington University in St. Louis, St. Louis, MO, and accepted by the Editorial Board February 23, 2015 (received for review August 26, 2014)

To adapt to a wide range of physically demanding environmental conditions, biological systems have evolved a diverse variety of robust skeletal architectures. One such example, *Euplectella aspergillum*, is a sediment-dwelling marine sponge that is anchored into the sea floor by a flexible holdfast apparatus consisting of thousands of anchor spicules (long, hair-like glassy fibers). Each spicule is covered with recurved barbs and has an internal architecture consisting of a solid core of silica surrounded by an assembly of coaxial silica cylinders, each of which is separated by a thin organic layer. The thickness of each silica cylinder progressively decreases from the spicule's core to its periphery, which we hypothesize is an adaptation for redistributing internal stresses, thus increasing the overall strength of each spicule. To evaluate this hypothesis, we created a spicule structural mechanics model, in which we fixed the radii of the silica cylinders such that the force transmitted from the surface barbs to the remainder of the skeletal system was maximized. Compared with measurements of these parameters in the native sponge spicules, our modeling results correlate remarkably well, highlighting the beneficial nature of this elastically heterogeneous lamellar design strategy. The structural principles obtained from this study thus provide potential design insights for the fabrication of high-strength beams for load-bearing applications through the modification of their internal architecture, rather than their external geometry.

structure–property relationship | structural biomaterial | biocomposite | variational analysis

Biological structural materials such as nacre, tooth, bone, and fish scales (1–9) often exhibit remarkable mechanical properties, which can be directly attributed to their unique structure and composition (10–15). Through the detailed analysis of these complex skeletal materials, useful design lessons can be extracted that can be used to guide the synthesis of synthetic constructs with novel performance metrics (16–20). The complex and mechanically robust cage-like skeletal system of the hexactinellid sponge *Euplectella aspergillum* has proved to be a particularly useful model system for investigating structure–function relationships in hierarchically ordered biological composites (21–25). The sponge is anchored to the sea floor by thousands of anchor spicules (long, hair-like skeletal elements), each of which measures ca. 50 μm in diameter and up to 10 cm in length (Fig. 1 *A* and *B*). The distal end of each anchor spicule is capped with a terminal crown-like structure and is covered with a series of recurved barbs that secure the sponge into the soft sediments of the sea floor (Fig. 1*C*). The proximal regions of these spicules are in turn bundled together and cemented to the main vertical struts of the skeletal lattice.

These spicules contain an elastically heterogeneous, lamellar internal structure and are composed of amorphous hydrated silica. Surrounding a thin organic axial filament, which is responsible for determining the spicule's core geometry, is a solid silica core. This core is further surrounded by an assembly of ca. 10–50 concentric cylinders (Fig. 1*D*), each of which is separated by a very thin organic interlayer (22), and previous studies have demonstrated that this design strategy contributes to a significant increase in work of fracture (22). These silica cylinders decrease in thickness from the spicule's core to the periphery (22–24) and, inspired by their internal geometric regularity, the goal of this study was to explore additional mechanical benefits of the spicule's laminated architecture. Specifically, we explored the possibility that the structural feature of decreasing silica cylinder thickness is an adaptation for increasing the strength of spicules under a wide range of external loading regimes.

To evaluate our hypothesis, we built a structural model for these spicules and compared the idealized sequence of silica cylinder radii from our model to the measured radii sequences from the native spicules. In our model, we quantify the spicule's ability to function as an effective structural element by its load capacity, which we define as the largest tensile force that the spicule can transmit from its surface barbs to the skeleton without failing. Because *E. aspergillum* is anchored into the sea floor, any loads on the sponge's body must be balanced by reaction forces supplied by the sediments. It is clear from the macroscale construction of the skeleton (22) that these reaction forces are transmitted directly to the skeleton via the anchor spicules. Although the distal region of each spicule that is located beneath the sediment surface is subjected to a diverse set of mechanical loads, from the shape and position of the surface barbs, we infer that the spicules are primarily loaded at the barbs by a system of forces that act in the proximo-distal direction (Fig. 1*C*).

In our model, the spicule's failure criterion is defined by the following three assumptions: (*i*) The onset of spicule failure begins when any of the individual silica cylinders fail or the spicule's core fails. (*ii*) An individual cylinder fails when the normal component of the traction σ_{33} on its cross-section exceeds its bulk tensile strength. The failure of the spicule's core is

Significance

The remarkable properties of biological structural materials can often be attributed to the composite arrangement of their constituents. This paper focuses on the high-aspect-ratio, load-bearing, glassy skeletal fibers (spicules) of the marine sponge *Euplectella aspergillum*. Considering that the spicules' internal architecture cannot be repaired or remodeled, we hypothesize that there is a connection between their internal structure and their strength. Using a newly developed structural mechanics model for composite beams, we demonstrate that the unique internal geometry that maximizes a beam's strength correlates well with the geometry observed in the native spicules. This bio-inspired design strategy for increasing a beam's strength has implications for a new generation of man-made structural materials.

Author contributions: J.C.W., J.A., and H.K. designed research; M.A.M., J.C.W., T.Z., and H.K. performed research; M.A.M. and H.K. analyzed data; and M.A.M., J.C.W., J.A., and H.K. wrote the paper.

The authors declare no conflict of interest.

This article is a PNAS Direct Submission. G.M.G. is a guest editor invited by the Editorial Board.

[1]To whom correspondence should be addressed. Email: haneesh_kesari@brown.edu.

This article contains supporting information online at www.pnas.org/lookup/suppl/doi:10.1073/pnas.1415502112/-/DCSupplemental.

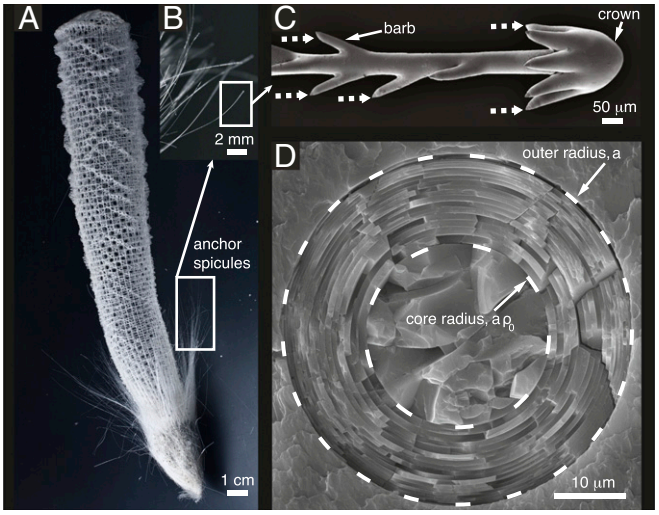

Fig. 1. (*A*) Photograph of a skeleton of *E. aspergillum* showing the tuft of root-like anchor spicules at the base. (*B*) A close-up of a group of anchor spicules. (*C*) A scanning electron microscope (SEM) image of the distal end of an anchor spicule, showing the spicule's terminal crown-like structure and its recurved barbs. The dashed arrows schematically denote the forces that we assume act on the spicule as it anchors the skeleton to the sea floor. Reproduced with permission from ref. 23. (*D*) SEM image of an anchor spicule's cross-section, taken at a smooth proximal region along the spicule's length.

similarly defined. And (*iii*) the cylinders and the core have the same bulk tensile strength σ_t^s.

Assumption *iii* contrasts with classical theories of strength in brittle structures, in which strength depends on size. For example, theories based on linear elastic fracture mechanics (LEFM) predict that strength scales as size$^{-1/2}$ (26–28). However, modern developments have brought attention to the fact that if a structure's characteristic dimension is smaller than a critical length scale, which is a characteristic of the structure's material and geometry, then strength no longer depends on size (14, 29). In *SI Text*, section S6 we show that the silica cylinder thicknesses are smaller than an estimate of the cylinders' critical length scale.

In traditional theories of homogeneous beams [e.g., Euler–Bernoulli (30)], σ_{33} is assumed to be an affine function over the beam's cross-section. As an extension, in our model, we allow σ_{33} to be a different affine function over the cross-section of each of the individual silica cylinders. Although the precise mechanical properties of the compliant organic interlayers have yet to be fully characterized, we incorporate their potential contributing effect into our model by assuming that σ_{33} can be discontinuous across adjacent silica cylinders. The assumption that the interlayers are compliant compared with the silica cylinders is supported through recent mechanical characterization of spicules from *Monorhaphis chuni* (31, 32), which is closely related to *E. aspergillum,* contains a similar bulk chemical composition (25), and is similarly laminated.

In line with our hypothesis that the spicule's internal structure enhances its strength in tensile and bending loading regimes, we set the free parameters in the affine functions characterizing σ_{33} on the spicule's cross-section Ω to be equal to the values at which the spicule's load capacity is maximized. Similarly, we set the radii of the silica cylinders to be equal to values that maximize the load capacity. The optimal-strength radii sequence thus designates this sequence of optimal values of the silica cylinder radii. In the present study, we provide a rigorous proof that in our model, the load capacity for the optimal-strength radii sequence is greater than the load capacity for any other possible sequence of radii.

The spicule's load capacity in our model is always greater than that of a homogeneous beam and increases with the number of silica cylinders up to a maximum gain of 25%. In a homogeneous Euler–Bernoulli beam, the outer region of Ω carries the greatest load, whereas the inner region carries the least. This is due to the affine variation of σ_{33} over Ω, for which σ_{33} attains a maximum at the periphery of Ω. Thus, per the failure criterion in our model, the homogeneous beam would fail when σ_{33} exceeds σ_t^s at the periphery. If σ_{33} varied more uniformly over Ω while still being greatest at the periphery, the structure would again fail when σ_{33} exceeds σ_t^s at the periphery. However, in this case, the net load transmitted across Ω (the load capacity) would be greater because the interior region of Ω would be transmitting a larger load. This is precisely the mechanism through which the load capacity in our spicule model is increased. By simultaneously allowing σ_{33} to be discontinuous and by increasing the number of silica cylinders, we effectively increase the uniformity of σ_{33} over Ω.

Remarkably, we find that the thicknesses in the optimal-strength radii sequence decrease from the spicule's core to the periphery, an observation consistent with measurements made on the actual spicules. We quantitatively compare the measured radii sequences with the optimal-strength radii sequence and also with several alternate radii sequences (*Discussion*, *Comparison of Measured and Optimal Radii Sequences*). One of these alternate sequences is from a different structural mechanics model in which the strength of the cylinders varies as thickness$^{-1/2}$. We find that the optimal-strength radii sequence describes the measured radii sequences the best.

The similarity of the optimal-strength radii sequence to the measured radii sequences supports our hypothesis that the spicule's internal structure is an adaptation to increase the spicule's load capacity. However, considering that knowledge regarding the formation of spicules in hexactinellid sponges is as yet incomplete, it cannot be ruled out whether other factors, such as growth processes, are also responsible for the spicule's decreasing-thickness lamellar structure.

Results

Measurements of Silica Cylinder Radii. The sectioned anchor spicules from *E. aspergillum* contained between 14 and 40 silica cylinders each. In most images, the complete boundaries of all of the cylinders were not easily identifiable due to the complex fracture patterns induced by sample sawing. Although this may have been the case, we were able to measure the radii of more than 80% of the total number of cylinders in more than 90% of the spicules. In the remaining 10% of the spicules, we succeeded in measuring at least 65% of the total number of cylinders. See *SI Text*, section S7 for details. We also ensured that in every image, the measured radii were from a consecutive set of silica cylinders starting from the innermost one, thus permitting the comparison of the measured radii sequences with the optimal-strength radii sequence from our model.

Consistent with previous observations (22–24), there was a distinct reduction in silica cylinder thickness from the spicule's core to its periphery (Fig. 2 and Fig. S1). See *SI Text*, section S7 for a statistical analysis of the cylinder thickness vs. cylinder number data.

Spicule's Load Capacity. We model the spicule as a tight, coaxial assembly of annular, cylindrical beams (30) with a single solid beam at its center. If the spicule fails at the transverse cross-section Ω, then the load capacity is equal to the tension T transmitted across Ω just before failure. Here we assume that the spicule transmits the greatest tension just before failure. The tension across Ω is

$$T = \int_{\Omega} \sigma_{33}\ dx_1 dx_2, \qquad [1]$$

where σ_{33} is a component of the Cauchy stress tensor in the orthonormal basis $\{\hat{\mathbf{e}}_i\}_{i=1,2,3}$. Note that Ω is the spicule's cross-section referred to in the deformed configuration. The vector $\hat{\mathbf{e}}_3$ is normal to Ω, and the vector $\hat{\mathbf{e}}_1$ points in the direction of the net bending moment on Ω. The origin is chosen to be the centroid of Ω and x_1, x_2 are the Cartesian coordinates in the $\hat{\mathbf{e}}_1$, $\hat{\mathbf{e}}_2$ directions, respectively (Fig. 3*A*).

As mentioned in the Introduction, we assume that the onset of spicule failure occurs when any of its cylinders fail or its core fails. A cylinder or the core fails when the maximum principal stress at any point within it exceeds the structure's bulk tensile strength. Because we treat each of the cylinders and the core as structural beams, the maximum principal stress at every point within the spicule is σ_{33}. Furthermore, we assume that the bulk tensile strength of each of the cylinders is the same. Because the cylinders' thicknesses vary from the core to the periphery, this last assumption of our failure criterion contrasts with the observation that the strength of ceramic structures typically depends on their size (26, 28).

However, we believe that this last assumption is justified for the following reason. According to Bažant's theory of stress redistribution and fracture energy release for scaling of structural strength (29), the strength σ_t^s of a quasi-brittle structure scales with its characteristic size D as

$$\sigma_t^s \propto \left(1 + \frac{D}{D_0}\right)^{-1/2}, \qquad [2]$$

where D_0 is a critical length scale, characteristic of the structure's geometry and material. When $D \gg D_0$, [2] asymptotes to the scaling law $\sigma_t^s \propto D^{-1/2}$ predicted by LEFM (26–28). And when $D \ll D_0$, the strength effectively becomes independent of D and can be taken to be a constant. We show in *SI Text*, section S6 that the silica cylinders lie in the regime where $D < D_0$, and therefore it is reasonable to assume that their strengths are the same.

Although the core's strength is expected to be smaller than that of the cylinders, our results change minimally regardless of whether the core's strength is different from or the same as that of the cylinders. For the sake of simplicity, in the following analysis we consider only the case in which the core's strength is the same as that of the cylinders. [We take the spicule's core radius $a\rho_0$ to be a constant in our analysis. Therefore, on taking the strength of the core to be different from that of the cylinders, only the expression for the load capacity given in [8] changes. The important results, namely the optimal-strength radii sequence given in [11]–[13] and the remarks in *Discussion*, *Remarks on the Optimal-Strength Radii Sequence*, do not change. Consequently, none of the conclusions drawn from the structural mechanics model are affected as a result of this assumption.] In summary, the failure criterion of our model stipulates that just before failure

$$\sigma_{33} \le \sigma_t^s \qquad [3]$$

at all points on Ω, with the equality holding for at least one point.

The precise variation of σ_{33} over the spicule's cross-section just before failure will depend on the constitutive behavior of the organic and silica phases, the mechanical behavior of the interfaces, and the forces acting on the spicule. Because we have limited information on these specific quantities, as a first-order approximation, we assume that σ_{33} on Ω just before failure can be described by an affine function in each of the silica cylinders. Specifically, numbering the silica cylinders starting with the spicule's core as $j = 0, \ldots, n$, we assume that just before failure σ_{33} on Ω in the jth silica cylinder has the form

$$\sigma_{33} = \left(\frac{x_2}{a\varrho_j} + \varepsilon_0\right), \qquad [4]$$

where a denotes the spicule's outer radius. We use [4] for modeling σ_{33} because it is the simplest form that allows a tension and a bending moment to be transmitted across Ω.

The symbols ϱ_j, $j = 0, \ldots, n$, and ε_0 denote positive, but otherwise arbitrary parameters. Note that while determining ϱ_j and ε_0 we allow σ_{33} to be discontinuous across adjacent silica cylinders. This type of stress discontinuity generally implies a slip or a tear in the material. However, in the spicules we believe that the apparent stress discontinuity across silica cylinders is accommodated by the large deformation of the relatively compliant organic interlayers. Allowing σ_{33} to be discontinuous across adjacent silica cylinders causes the load capacity to depend on

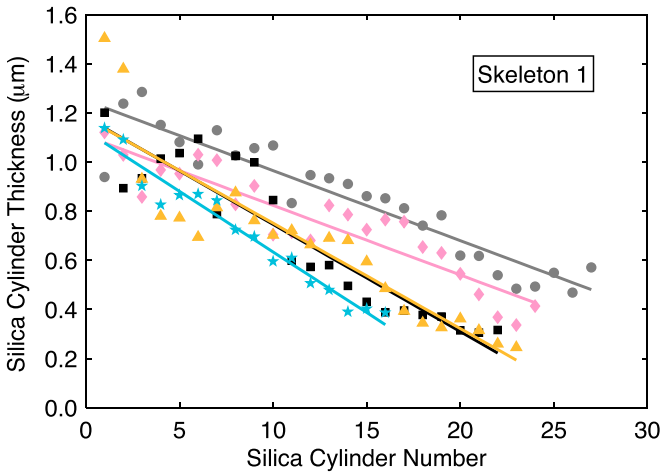

Fig. 2. Thicknesses vs. cylinder number data for five skeleton 1 spicules. The solid lines shown are linear fits to the data.

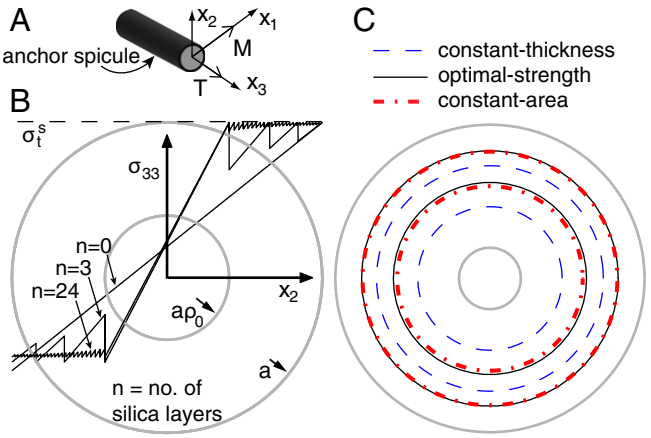

Fig. 3. Spicule model and results. (*A*) The spicule model coordinate system and loading configuration. (*B*) σ_{33} on Ω when the model transmits a tension equal to its peak load capacity $\hat{\mathcal{L}}^n$, for different n. The stress component σ_{33} is computed using [4] for the optimal values of ϱ_j and ε_0 given by [S17] and [S18], for $G = 1$. (*C*) The optimal-strength radii sequence given by [11]–[13] for $n = 3$. For comparison, two other radii sequences in which the cylinders' areas and thickness are, respectively, constant are also shown. The core radius ρ_0 is 0.4 in *B* and 0.2 in *C*.

the radii of the silica cylinders and to be larger than that of a homogeneous beam.

Using [4], the tension T and bending moment $M = \int_\Omega \sigma_{33} x_2 \; d\Omega$ on Ω are

$$T = \pi a^2 \varepsilon_0, \qquad [5]$$

$$M = \frac{\pi a^3}{4}\left[\frac{\rho_0^4}{\varrho_0} + \frac{(\rho_1^n)^4 - (\rho_0)^4}{\varrho_1} + \sum_{j=2}^{n} \frac{(\rho_j^n)^4 - (\rho_{j-1}^n)^4}{\varrho_j}\right], \qquad [6]$$

where $\rho_j^n, j = 1, \ldots, n$, is defined such that $a\rho_j^n$ is the outer radius of the jth silica cylinder and $a\rho_0$ is the radius of the spicule's core. We take ρ_0 to be nonnegative and less than unity. For $j = n$, $a\rho_n^n$ is the spicule's outer radius a, and therefore ρ_n^n is always equal to unity. We take the spicule's core and outer radius to be fixed in our analysis and refer to the outer radii of the internal silica cylinders through the vector $a\boldsymbol{\rho}^n = a(\rho_1^n, \ldots, \rho_{n-1}^n)$. For $\boldsymbol{\rho}^n$ to be well defined it is necessary that $n > 1$.

It might appear from [5] that T depends only on our choice of ε_0. In fact, T depends on all of the constants $\mathbf{x} = (\varrho_0, \ldots, \varrho_n, \varepsilon_0)$ and the radii sequence $\boldsymbol{\rho}^n$, because M depends on ϱ_j and $\boldsymbol{\rho}^n$, and

$$T = \frac{M}{Ga}, \qquad [7]$$

where G is a positive constant. Constraint [7] follows from the fact that both T and M on Ω arise from the same set of forces at the surface barbs. Further details on [7] are given in *SI Text*, section S1.1. In line with our hypothesis that the spicule's internal structure is an adaptation that enhances its anchoring ability, we fix $\mathbf{x}$ and $\boldsymbol{\rho}^n$ to be equal to values at which the load capacity is maximized. Because $\mathbf{x}$ and $\boldsymbol{\rho}^n$ are unrelated, we can derive their optimal values independently. We determine the optimal values of $\mathbf{x}$ by maximizing T subject to the constraints [3] and [7] (*SI Text*, section S1.2). We denote the load capacity corresponding to the optimal values of $\mathbf{x}$ as $\mathcal{L}^n$, found by substituting the optimal values of $\mathbf{x}$ in [5] and [6],

$$\mathcal{L}^n[\boldsymbol{\rho}^n] = \frac{\pi a^2 \sigma_t^s}{4} \frac{4\mathcal{M}^n[\boldsymbol{\rho}^n]}{4G + \mathcal{M}^n[\boldsymbol{\rho}^n]}, \qquad [8]$$

where

$$\mathcal{M}^n[\boldsymbol{\rho}^n] = \rho_0^3 + \frac{(\rho_1^n)^4 - (\rho_0)^4}{\rho_1^n} + \sum_{j=2}^{n} \frac{(\rho_j^n)^4 - (\rho_{j-1}^n)^4}{\rho_j^n}. \qquad [9]$$

We then determine the optimal value of $\boldsymbol{\rho}^n$ by maximizing $\mathcal{L}^n$ subject to the constraints that the core radius $a\rho_0$, outer radius a, and the number of silica cylinders n are fixed and that $\boldsymbol{\rho}^n$ belongs to the set

$$\mathcal{B}^n = \left\{\boldsymbol{\rho}^n \in \mathbb{R}^{n-1} : \rho_0 \le \rho_1^n,\ \rho_{j-1}^n \le \rho_j^n,\ j = 2, \ldots,\ n\right\}, \qquad [10]$$

where $\mathbb{R}^{n-1}$ is the $n-1$-dimensional Euclidean space. For the cylinder thicknesses to be positive, it is necessary that $\boldsymbol{\rho}^n$ belong to $\mathcal{B}^n$. In *SI Text*, section S2 we show that $\mathcal{L}^n$ achieves the global maximum over the set $\mathcal{B}^n$ uniquely at $\boldsymbol{\rho}^n = (\hat{\rho}_1^n, \ldots, \hat{\rho}_{n-1}^n)$, where

$$\hat{\rho}_j^n = \prod_{k=j}^{n-1} \alpha_k, \quad j = 1, \ldots, n-1, \qquad [11]$$

and α_k are terms of the sequence $(\alpha_k)_{k=0}^{\infty}$, where

$$\alpha_0 = \frac{\rho_0}{\alpha_1 \alpha_2 \cdots \alpha_{n-1}}, \qquad [12]$$

$$\alpha_k = \frac{3}{4} + \frac{\alpha_{k-1}^4}{4}, \qquad [13]$$

for $k > 0$. We refer to $(\hat{\rho}_1^n, \ldots, \hat{\rho}_{n-1}^n) = \hat{\boldsymbol{\rho}}^n$ as the optimal-strength radii sequence and the load capacity $\mathcal{L}^n[\hat{\boldsymbol{\rho}}^n]$ corresponding to this sequence as the peak load capacity $\hat{\mathcal{L}}^n$.

Discussion

Remarks on the Optimal-Strength Radii Sequence.

i) By comparing the peak load capacity $\hat{\mathcal{L}}^n$ with load capacities corresponding to three other radii sequences (Fig. 4), it can be seen that $\hat{\mathcal{L}}^n$ is always the largest. In addition, it should be noted that the load capacities corresponding to the optimal-strength radii sequence and the radii sequence in which the cylinder cross-sectional areas are constant are almost indistinguishable. This is because the optimal-strength and the constant-area radii sequences are very similar to each other. For ρ_0 and n close to the values measured in the four skeletons (Table S1), the Euclidean distance (33) between the optimal-strength and constant-area radii sequences is less than 4% of the diameter of $\mathcal{B}^n$. The closeness of the optimal-strength and constant-area radii sequences can also be seen in Fig. 3*C*.

ii) The load capacity $\hat{\mathcal{L}}^{n+1} > \hat{\mathcal{L}}^n$ for all n, that is, the peak load capacity, always increases with the number of silica cylinders (Fig. 4). We derive this result in *SI Text*, section S4.1. However, it is generally not true that $\mathcal{L}^{n+1}[\boldsymbol{\rho}^{n+1}] > \mathcal{L}^n[\boldsymbol{\rho}^n]$ for arbitrary types of radii sequences.

iii) We studied the aggregate load capacity for a set of spicules having randomly chosen radii sequences and found that it also increases with n. We also found that, at any given n, the

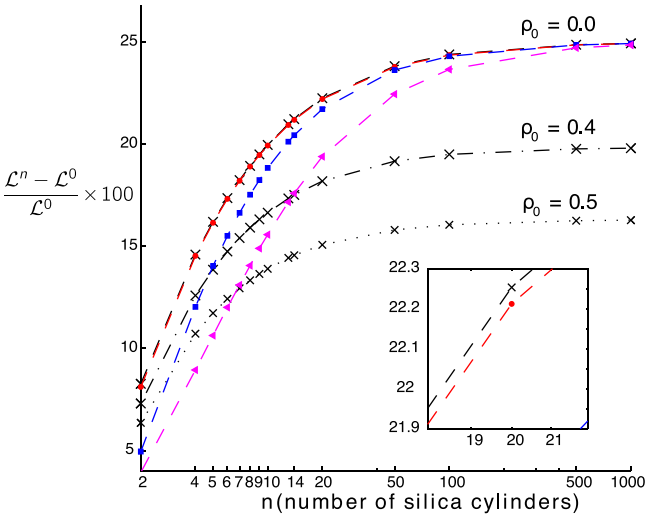

Fig. 4. Percentage increase in the load capacity $\mathcal{L}^n[\boldsymbol{\rho}^n]$ (defined in [8]) as a function of the total number of silica cylinders n plotted on a semilog scale. All calculations are for $G = 1$. The black crosses correspond to $\boldsymbol{\rho}^n = \hat{\boldsymbol{\rho}}^n$, the optimal-strength radii sequence, for $\rho_0 = 0.0$, 0.4, and 0.5. The red circles correspond to radii sequences in which the silica cylinders' cross-sectional areas are constant and the blue squares correspond to radii sequences in which the silica cylinders' thicknesses are constant. For each n, the pink triangle denotes the aggregate load capacity of a set of 10^4 randomly generated radii sequences; the SEs are very small ($< 3.2151 \times 10^{-4}$); therefore, we do not show them as error bars. In the constant-area, constant-thickness, and aggregate load capacity plots $\rho_0 = 0.0$. *Inset* shows a close-up of the plots around the region $n = 20$.

aggregate load capacity is smaller than the peak load capacity. However, the difference becomes vanishingly small as n becomes large. For example, setting $\rho_0 = 0$ we found that when $n < 20$, the aggregate load capacity is smaller than $\hat{\mathcal{L}}^n$ by about 20%. However, when $n > 100$, the difference between the aggregate load capacity and $\hat{\mathcal{L}}^n$ becomes less than 1% (Fig. 4). These results show that the strategy of increasing the load capacity by partitioning the load-bearing material into several coaxial cylinders is quite robust.

iv) Numerically, for a wide range of n we found that $\hat{\mathcal{L}}^n$ is always greatest when $\rho_0 = 0$. Similarly, for $\rho_0 = 0$ we found that $\hat{\mathcal{L}}^n$ asymptotes to $\pi a^2 \sigma_t^s/(3G+1)$ as n becomes large (Fig. 4). Setting $n = 1$ and $\rho_0 = 0$ in [**8**] and [**9**] we found that the load capacity of a homogeneous silica beam is $\pi a^2 \sigma_t^s/(4G+1)$. Based on these calculations, it can be shown that the spicule's internal structure can increase its load capacity by a maximum of 25% over that of a homogeneous beam.

v) We found that the thicknesses corresponding to $\hat{\boldsymbol{\rho}}^n$ decrease from the spicule's core to its periphery. The proof of this result is given in *SI Text*, section S4.2.

Comparison of Measured and Optimal Radii Sequences. In our model, the thicknesses corresponding to $\hat{\boldsymbol{\rho}}^n$ decrease from the spicule's core to its periphery. Qualitatively, this finding is consistent with our measurements of cylinder thicknesses in the native spicules (Fig. 2 and Fig. S1). To quantify the closeness of the measured radii sequences to the optimal-strength radii sequence we compute the metric

$$d = \frac{\left[(r_0 - a\rho_0)^2 + \sum_{j=1}^{p}\left(r_j - a\hat{\rho}_j^n\right)^2\right]^{1/2}}{\left\langle\left[\sum_{j=0}^{p}\left(r_j - \chi_j\right)^2\right]^{1/2}\right\rangle} \qquad [14]$$

for each of the spicules. In [**14**], the term r_0 is the measured radius of the spicule's core and $r_1, \ldots, r_p$ are the measured radii of the first p consecutive silica cylinders. Given $a\rho_0$ and α_0, $a\hat{\rho}_j^n$, $j = 1 \ldots p$, can be computed using [**11**] and [**13**]. Thus, there are two free parameters $a\rho_0$ and α_0 in [**14**], which we choose to make d as small as possible. The denominator of [**14**] is the average of the Euclidean distance between the measured radii sequence r_j and a monotonically increasing sequence χ_j of p numbers lying between r_0 and r_p, computed for 10^4 randomly generated χ_j. Thus, if $d < 1$, the test sequence $\hat{\rho}_j^n$ fits the measured sequence better than a randomly chosen sequence of radii. For reference, we also computed d with $\hat{\boldsymbol{\rho}}^n$ replaced by radii sequences for which the cylinders' cross-sectional areas and thicknesses are, respectively, constant. We chose $a\rho_0$ and the area (respectively thickness) of the cylinders in the constant-area (respectively constant-thickness) sequence to make d as small as possible. The means and SEs of d for the optimal-strength, constant-area, and constant-thickness sequences are shown in Table 1 for the four skeletons examined. The fitted radii sequences corresponding to a representative measured sequence from skeleton 1 are shown in Fig. 5.

Table 1. Metric $d \times 100$, mean ± SE

Skeleton	1	2	3	4
Optimal strength	19.3 ± 1.5	17.7 ± 1.7	21.6 ± 1.5	23.3 ± 2.0
Constant area	22.8 ± 2.7	20.2 ± 2.4	18.3 ± 2.2	28.4 ± 3.0
Constant thickness	29.0 ± 1.5	26.2 ± 1.4	30.7 ± 1.4	30.4 ± 1.4
Controlling flaw, $a\tau_n^n = 0.30$ μm	74.3 ± 7.1	73.0 ± 6.2	59.2 ± 4.9	144.1 ± 34.3

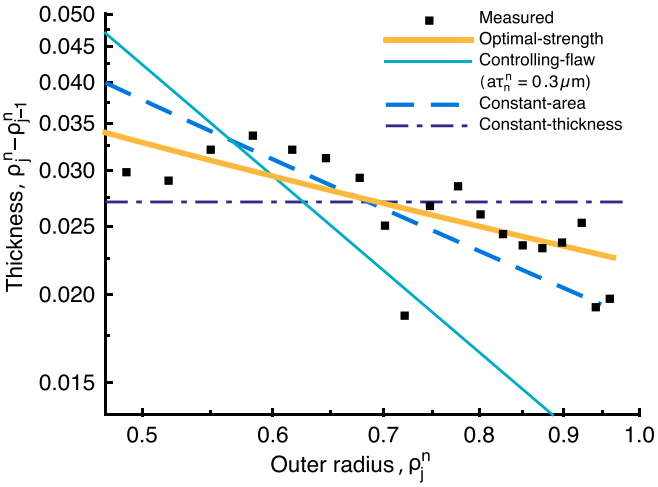

Fig. 5. Variation of the dimensionless thickness with the dimensionless outer radius of the silica cylinders on a log–log scale. The best-fit radii sequences from models discussed in *Discussion, Comparison of Measured and Optimal Radii Sequences* are shown along with the corresponding measured radii sequence from a representative spicule from skeleton 1.

We find that the mean values of d for the constant-area and optimal-strength radii sequences are smaller than for the constant-thickness radii sequence in each of the skeletons. Although the mean value of d for the optimal-strength radii sequence is slightly smaller than that for the constant-area radii sequence in skeletons 1, 2, and 4, these differences are not statistically significant. Therefore, we conclude that the optimal-strength and the constant-area radii sequences correlate equally well with the measured radii sequences and better than the constant-thickness radii sequence.

An alternate mechanics model based on the idea of controlling flaws has been put forward to explain the trend of decreasing thicknesses in the spicule's internal structure (32). In this alternate model σ_{33} is assumed to vary affinely over Ω and the load capacity is maximized by varying the cylinder thicknesses subject to the constraint that each cylinder's strength be greater than the maximum value of σ_{33} over its cross-section. This idea along with the scaling of strength predicted by LEFM implies that the sequence of radii should vary as

$$\rho_{j-1}^n = \rho_j^n - \frac{(1 + 1/4G)^2 \tau_n^n}{\left(\rho_j^n + 1/4G\right)^2}, \qquad [15]$$

where τ_n^n is the dimensionless thickness $1 - \rho_{n-1}^n$ of the outermost cylinder. Eq. **15** is derived in *SI Text*, section S5. We compute d by replacing $\hat{\rho}_j^n$ with the controlling-flaw radii sequence given in [**15**] and choosing $a\rho_p^n$ and G so that it is as small as possible. The computed values of d for various discrete τ_n^n are shown in Table S2. The results corresponding to the τ_n^n that produced the smallest d value are also shown in Table 1. As can be noted from Table 1 and Fig. 5, the measured radii sequences compare much better to our optimal-strength radii sequence than to the controlling-flaw radii sequence. In fact, the controlling-flaw radii sequence does not even fit as well as the constant-thickness sequence.

These results demonstrate that the spicule's internal structure is consistent with our model, supporting our hypothesis that the internal structure is an adaptation aimed at increasing the spicule's load capacity.

It is important to note that, although our results are very encouraging, they are far from a confirmation that mechanical optimization is the only factor contributing to the spicule's design. Some architectural features of biological structures are merely a consequence of the growth processes through which the

structures are formed and have no obvious functional implications, e.g., growth rings in fish scales (34). Despite previous efforts (35), knowledge regarding the detailed mechanisms underlying hexactinellid spicule formation is still incomplete and therefore, at this stage, it cannot be ruled out whether other factors, such as growth processes, are also responsible for the spicule's decreasing thickness lamellar structure. Even more importantly, many biological skeletal elements are inherently multifunctional and have evolved the ability to perform a variety of tasks in addition to their mechanical ones. In particular, it has been shown that sponge spicules have exceptional fiberoptical properties (21, 23, 36). Currently, we cannot be certain that the spicule's internal architecture contributes solely to its mechanical function or whether it has additional (e.g., light transmission) benefits. However, whether the spicule's architecture is a simple outcome of its growth process or is specifically optimized for multifunctionality, it clearly offers the sponge skeleton an exceptional mechanical advantage.

Similarly, it is also possible that the spicule's internal architecture is connected to a different metric of the spicule's mechanical efficiency, such as the failure curvature—the largest curvature the spicule can withstand without failing.

Concluding Remarks

To thoroughly test our hypothesis, it is necessary to confirm some of our model's key assumptions, such as (*i*) that the spicule fails according to the failure criterion outlined in *Results*, *Spicule's Load Capacity* and (*ii*) just before failure, σ_{33} on Ω varies in an optimal fashion so that the spicule's load capacity is as large as possible.

Although the information required to validate these key assumptions is currently unavailable, additional measurements of the elastic properties and failure behavior of the spicules at different length scales will aid in the further refinement of our structural model.

As a consequence of the key assumption *ii*, our model predicts that the peak values of σ_{33} in each of the silica cylinders will all be equal to the failure stress σ_t^s at the onset of failure (Fig. 3*B*). This prediction can be interpreted to mean that the cylinders will all fail at once. Considering that our model is an idealization and that it is not constructed with the goal of capturing the failure process, we do not expect this interpretation to be accurate. We believe that the silica cylinders will fail progressively, as was observed in spicules from related species (25, 32, 37).

In traditional engineering design, the specific strength of load-bearing structural elements is increased by varying their external geometry. For example, for small deformation of a homogeneous beam, σ_{33} on Ω varies as $\sigma_{33} = Mx_2/I$ when Ω is symmetric about the $\hat{\mathbf{e}}_1$ direction (30). Here I is the second moment of inertia of Ω about the $\hat{\mathbf{e}}_1$ direction. As a result, a beam's specific strength can be maximized by varying the shape of Ω to make the beam's dimension in the $\hat{\mathbf{e}}_2$ direction and the area of Ω as small as possible, while making the beam's inertia I as large as possible. In contrast, the spicules discussed here can be seen as an inspiration for new design strategies in which a structure's specific strength can be increased by varying its internal elastic composition. For example, one could envision composite beams whose internal elastic heterogeneity results in a stress distribution that becomes increasingly uniform as the beam deforms.

Materials and Methods

Anchor spicules from four individual *E. aspergillum* skeletons were embedded in Spurr's resin, cross-sectioned, and imaged with a Tescan Vega scanning electron microscope (Fig. 1*D*). From the resulting images, we measured the sequence of silica cylinder radii by fitting circles to the cylinder boundaries starting with the spicule's core (Fig. S2). We also measured the number of silica cylinders and the outer radius for each of the 116 spicules examined (Table S1). For details see *SI Text*, section S7.

ACKNOWLEDGMENTS. We thank Prof. Huajian Gao for helpful discussions. This work was supported by the National Science Foundation through Materials Research Science and Engineering Centers Program DMR-0520651 at Brown University, Materials Research Science and Engineering Centers Program DMR-1420570 at Harvard University, and the Korean Institute of Machinery and Materials–Brown Nano and Micromechanics for Disaster Mitigation and Technological Reliability project.

1. Jackson AP, Vincent JFV, Turner RM (1988) The mechanical design of nacre. *Proc R Soc Lond B Biol Sci* 234(1277):415–440.
2. Currey JD (1977) Mechanical properties of mother of pearl in tension. *Proc R Soc Lond B Biol Sci* 196(1125):443–463.
3. Nalla RK, Kinney JH, Ritchie RO (2003) On the fracture of human dentin: Is it stress- or strain-controlled? *J Biomed Mater Res A* 67(2):484–495.
4. Currey JD (2003) How well are bones designed to resist fracture? *J Bone Miner Res* 18(4):591–598.
5. Weiner S, Wagner HD (1998) The material bone: Structure-mechanical function relations. *Annu Rev Mater Sci* 28(1):271–298.
6. Fratzl P, Gupta HS, Paschalis EP, Roschger P (2004) Structure and mechanical quality of the collagen–mineral nano-composite in bone. *J Mater Chem* 14(14):2115–2123.
7. Gupta HS, et al. (2006) Cooperative deformation of mineral and collagen in bone at the nanoscale. *Proc Natl Acad Sci USA* 103(47):17741–17746.
8. Browning A, Ortiz C, Boyce MC (2013) Mechanics of composite elasmoid fish scale assemblies and their bioinspired analogues. *J Mech Behav Biomed Mater* 19:75–86.
9. Yang W, et al. (2013) Structure and fracture resistance of alligator gar (*Atractosteus spatula*) armored fish scales. *Acta Biomater* 9(4):5876–5889.
10. Vincent JFV (1990) Stiff materials – fibrous composites. *Structural Biomaterials*, ed Duncan F (Princeton Univ Press, Princeton), Revised Ed, pp 126–163.
11. Mayer G (2005) Rigid biological systems as models for synthetic composites. *Science* 310(5751):1144–1147.
12. Chen P-Y, et al. (2008) Structure and mechanical properties of selected biological materials. *J Mech Behav Biomed Mater* 1(3):208–226.
13. Ritchie RO (2011) The conflicts between strength and toughness. *Nat Mater* 10(11):817–822.
14. Gao H, Ji B, Jäger IL, Arzt E, Fratzl P (2003) Materials become insensitive to flaws at nanoscale: Lessons from nature. *Proc Natl Acad Sci USA* 100(10):5597–5600.
15. Dunlop JWC, Fratzl P (2010) Biological composites. *Annu Rev Mater Res* 40:1–24.
16. Munch E, et al. (2008) Tough, bio-inspired hybrid materials. *Science* 322(5907): 1516–1520.
17. Vincent JFV (1990) Biomimetic and intelligent materials. *Structural Biomaterials*, ed Duncan F (Princeton Univ Press, Princeton), Revised Ed, pp 204–209.
18. Launey ME, et al. (2009) Designing highly toughened hybrid composites through nature-inspired hierarchical complexity. *Acta Mater* 57(10):2919–2932.
19. Tomisa AP, et al. (2011) Nanotechnology approaches to improve dental implants. *Int J Oral Maxillofac Implants* 26(Suppl):25–44, discussion 45–49.
20. Porter MM, Mckittrick J, Meyers MA (2013) Biomimetic materials by freeze casting. *JOM* 65(6):720–727.
21. Sundar VC, Yablon AD, Grazul JL, Ilan M, Aizenberg J (2003) Fibre-optical features of a glass sponge. *Nature* 424(6951):899–900.
22. Weaver JC, et al. (2007) Hierarchical assembly of the siliceous skeletal lattice of the hexactinellid sponge *Euplectella aspergillum*. *J Struct Biol* 158(1):93–106.
23. Aizenberg J, Sundar VC, Yablon AD, Weaver JC, Chen G (2004) Biological glass fibers: Correlation between optical and structural properties. *Proc Natl Acad Sci USA* 101(10): 3358–3363.
24. Aizenberg J, et al. (2005) Skeleton of Euplectella sp.: Structural hierarchy from the nanoscale to the macroscale. *Science* 309(5732):275–278.
25. Weaver JC, et al. (2010) Unifying design strategies in demosponge and hexactinellid skeletal systems. *J Adhes* 86(1):72–95.
26. Griffith AA (1921) The phenomena of rupture and flow in solids. *Philos Trans R Soc Lond, A Contain Pap Math Phys Character* 221(582-593):163–198.
27. Green DJ (1998) Brittle fracture. *An Introduction to the Mechanical Properties of Ceramics*, Cambridge Solid State Science Series (Cambridge Univ Press, Cambridge, UK), pp 210–218.
28. Lawn BR (1993) *Fracture of Brittle Solids* (Cambridge Univ Press, Cambridge, UK), 2nd Ed, pp 1–14, 328–334, 350–353.
29. Bažant ZP (2005) *Scaling of Structural Strength* (Butterworth-Heinemann, Oxford), pp 3–27.
30. Gere JM, Timoshenko SP (1997) Stresses in beams. *Mechanics of Materials Second SI Edition* (PWS Publishing, Boston), pp 220–232.
31. Zlotnikov I, et al. (2013) In situ elastic modulus measurements of ultrathin protein-rich organic layers in biosilica: Towards deeper understanding of superior resistance to fracture of biocomposites. *RSC Adv* 3(17):5798–5802.
32. Miserez A, et al. (2008) Effects of laminate architecture on fracture resistance of sponge biosilica: Lessons from nature. *Adv Funct Mater* 18(8):1241–1248.
33. Marsden JE, Hoffman MJ (1993) The real line and Euclidean n-space. *Elementary Classical Analysis* (WH Freeman, San Francisco), pp 19–20.
34. Thompson DW (1942) On concretions, spicules, and spicular structures. *On Growth and Form: A New Edition* (Cambridge Univ Press, Cambridge, UK), pp 665–666.
35. Leys SP (2003) Comparative study of spiculogenesis in demosponge and hexactinellid larvae. *Microsc Res Tech* 62(4):300–311.
36. Cattaneo-Vietti RG, et al. (1996) Optical fibres in an antarctic sponge. *Nature* 383: 397–398.
37. Wang XH, et al. (2009) Giant basal spicule from the deep-sea glass sponge Monorhaphis chuni: Synthesis of the largest bio-silica structure on Earth by silicatein. *Front Mater Sci China* 3(3):226–240.